Elastic sheets on Winkler foundations: Indentation stiffness and nonlinearities

Erteng Chen [ID], Zhaohe Dai [ID] *

Department of Mechanics and Engineering Science, State Key Laboratory for Turbulence and Complex Systems, College of Engineering, Peking University, Beijing 100871, China

ARTICLE INFO

ABSTRACT

The indentation of thin sheets on Winkler's mattress or elastic foundations offers valuable opportunities to gain quantitative insights into the mechanical properties of both the material and its interface. However, interpreting indentation data is complicated by the interplay of plate bending, sheet pre-tension, and foundation deformation. The challenges are further amplified in recently developed nanoindentation techniques for small-scale systems, such as 2D materials and cell membranes, where indenter size, shape, and foundation nonlinearity have been found to influence the results significantly. Here, we address these challenges by investigating a generalized indentation problem involving a pre-tensioned elastic sheet on a mattress foundation, considering both punch and spherical indenters. By linearizing the Föppl–von Kármán equations and the elastic foundation under small indentation depth, we obtain a set of asymptotic solutions that quantify the effects of pre-tension and indenter geometry on indentation stiffness. These solutions show excellent agreement with numerical solutions in various parameter regimes that we classify. We also discuss sources of nonlinearities arising from the kinematics in sheet stretching and the evolving contact radius in spherical indentation. The results should be of direct use for the nanometrology of layered materials where indentation remains one of the most accessible techniques for characterizing mechanical properties at small scales.

1. Introduction

Thin film/substrate systems are ubiquitous in nature and engineering settings across different scales: from protective layers used to prevent wear and corrosion (Awang et al., 2019), to coatings that enhance the optical and thermal properties of bulk materials (Raut et al., 2011; Di Leo et al., 2014), and even to biological membranes like cell membranes that encapsulate cytoplasm (Yang and Hinner, 2015). In recent years, small-scale thin film/substrate systems have attracted particular attention due to their applications in microelectronic packaging (Nase et al., 2009), transistors (Zschieschang et al., 2022; Wang et al., 2025a), nanogenerators (Feng et al., 2018) and nanosensors (Hwang et al., 2015; Li et al., 2024a). Within these applications, the mechanical response of the substrate-supported thin films often plays an important role in the design, operation, and functionality of the system (Freund and Suresh, 2004). To test such responses, indentation experiments have been developed as one of the most important techniques due to their in-situ, non-destructive nature (see the review by Cao and Gao, 2019). For example, with well-developed atomic force microscopy (AFM), one can obtain highly resolved indentation force–displacement curves, which can provide valuable opportunities

to quantify the mechanical properties of thin films and their interfaces with the supporting substrate (Zhang et al., 2018; Yu and Dai, 2024).

Although the mechanics of film/substrate indentation have been extensively studied in various configurations and material laws (Bhattacharya and Nix, 1988; Freund and Suresh, 2004), recent cutting-edge experiments on 2D materials and cell membranes have introduced new factors to be explored (Gao et al., 2015, 2018; Cellini et al., 2018; Mandriota et al., 2019). A notable example is depicted in Fig. 1a, where few-layer graphene sheets rest on a SiC substrate with a separation of only a few angstroms (Gao et al., 2015; Wang et al., 2025b). This equilibrium spacing is governed by the van der Waals (vdW) forces acting between the sheet and the substrate (Israelachvili, 2011). In these experiments, the indentation depth is kept well below the equilibrium spacing, ensuring that the work done by the indentation load is mainly stored as elastic energy within the sheet and as vdW potential at the sheet–substrate interface (Gao et al., 2015, 2018). As a result, the problem becomes an elastic sheet resting on a nonlinear elastic foundation given by the vdW interactions. Another example, shown in Fig. 1b, involves an indentation applied to a tensioned cell membrane supported by a layer of spring-like cytoplasm (Mandriota
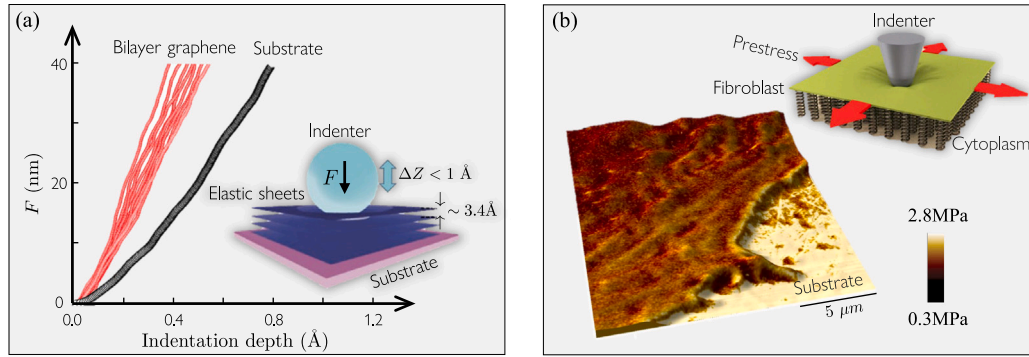

Fig. 1. (a) Experimental indentation curves in bilayer epitaxial Graphene (red), and SiC (black) (Source: Gao et al., 2018). The inset shows the schematic illustration of the contact model assumed in this angstrom-indentation method (Source: Cellini et al., 2018). (b) Effective elastic modulus (superimposed to the surface topography) acquired from the indentation of human umbilical vein endothelial cells. The inset illustrates the cellular indentation model, where the green surface represents the tensioned fibroblast cell cortex and the springs denote the elastic response of the cytoplasm layer under the cortex (Source: Mandriota et al., 2019).

et al., 2019). In both cases, the indentation force–depth curves can be readily measured; however, a key challenge is understanding what governs the indentation force–depth relation for an elastic sheet on a (nonlinear) foundation.

In the indentation experiments presented in Fig. 1, the nonlinear response of thin sheets introduces significant challenges in accurately interpreting the indentation data (Mansfield, 1989). Furthermore, a range of experimental factors must be carefully accounted for, including foundation nonlinearity, indenter geometry and size, as well as the ubiquitous presence of pre-tension in substrate-supported sheets, such as in-plane tension in cell cortices and residual stress in transferred 2D materials (Dai et al., 2019, 2020). These complexities markedly constrain the applicability of existing contact models for indenting elastic films on elastic slabs (Barber, 2018; Ding et al., 2023; Yuan et al., 2023). When both material response and elastic foundation are linearized, however, the system resembles plates on Winkler foundations or thin coatings (Chandler and Vella, 2020b), where indentation solutions have been extensively analyzed under various loading conditions (for a comprehensive review, see Dillard et al., 2018). Recent studies on pre-tensioned thin sheets floating on water (see Box et al., 2017) have further considered the geometrical nonlinearity in elastic sheets under point loading. Nonetheless, in small-scale experiments (e.g., Gao et al., 2018; Mandriota et al., 2019), even a probe size of just a few nanometers can significantly affect indentation results (Chandler and Vella, 2020a). A quantitative understanding of how sheet elasticity, indenter geometry, size, and pre-tension affect experimental outcomes is essential, yet remains underexplored in the literature. As a result, prior experiments (such as Gao et al., 2015, 2018; Mandriota et al., 2019) have been interpreted using approximate models that neglect many of these subtleties—an approach not yet fully justified.

This work aims to elucidate the indentation force–depth relations for a elastic film on a nonlinear foundation, with a particular focus on how the indentation stiffness relates to the sheet's mechanical properties, pre-tension, and indenter geometry. We present several new asymptotic solutions that could be useful in interpreting previous experiments. The paper is structured as follows: In Section 2, we introduce the governing equations and nondimensionalization to describe the indentation of films on foundations, along with a brief review of indentation stiffness for point loading. In Section 3, we examine angstrom-scale indentation of 2D materials as a case study to explore the analytical expression and asymptotic behavior of the indentation stiffness for a cylindrical indenter, quantifying the influence of film pre-tension and indenter radius. We also discuss the conditions under which geometric nonlinearity arises and assess the applicability of our linearized theory. In Section 4, we examine indentation behavior for a spherical indenter and several asymptotic results under small
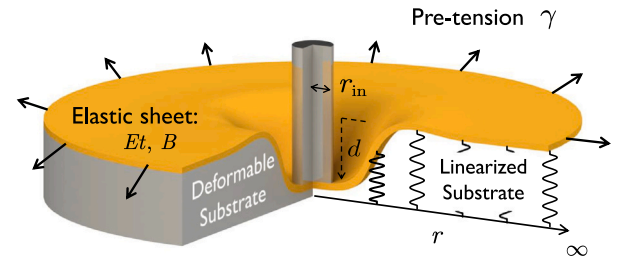
Fig. 2. Schematic illustration of the indentation of an elastic sheet on a linear, elastic foundation of stiffness of K_{sub} discussed in Section 2.1.2. The source of the linear foundation could be water (Box et al., 2017), thin compressible substrate (Dillard et al., 2018), or linearized vdW interactions (Gao et al., 2014).

indentation depth. In Section 5, we develop an equivalent method to calculate indentation stiffness for multilayer structures under punch loading. Finally, Section 6 provides a summary and conclusions of our work.

2. The generalized model

In this section, we present a generalized indentation model for thin sheets on elastic foundations that are consistent with previous experimental settings (Gao et al., 2018; Mandriota et al., 2019). To facilitate analytical progress, we adopt a linearized Winkler foundation model (Dillard et al., 2018; Kerr, 1964) and examine the indentation response of the system by focusing on small loads.

2.1. Theoretical setting

2.1.1. Governing equations

We consider an elastic sheet with Young's modulus E, thickness t, and bending stiffness B, resting on an elastic foundation, as illustrated in Fig. 2. In the context of geometric nonlinearity and Kirchhoff assumptions, we use axisymmetric Föppl–von Kármán equations to describe the vertical deflection w of the sheet, where upward displacement is defined as positive (Mansfield, 1989). The first equation introduces the vertical equilibrium:

$$B\nabla_r^2\nabla_r^2 w - \frac{1}{r}\frac{\mathrm{d}}{\mathrm{d}r}\left(\frac{\mathrm{d}\varphi}{\mathrm{d}r}\frac{\mathrm{d}w}{\mathrm{d}r}\right) + q = -f(r), \tag{2.1}$$

where $\nabla_r^2 g = \frac{\mathrm{d}^2 g}{\mathrm{d}r^2} + \frac{1}{r}\frac{\mathrm{d}g}{\mathrm{d}r}$ is the 2D axisymmetric Laplacian. In Eq. (2.1), q represents the restoring force from the substrate, which is explained in detail in Section 2.1.2. Given that we only solve for the film deformation outside the contact edge $r = a$, the force exerted by the

indenter can be thus expressed as: $f(r) = \frac{F\delta(r-a)}{2\pi r}$, where $\delta(r)$ is a Dirac delta function and F is the total indentation force. Also, we use Airy stress function φ with $N_r = \frac{1}{r}\frac{d\varphi}{dr}$ and $N_\theta = \frac{d^2\varphi}{dr^2}$ so that the in-plane equilibrium equation is automatically satisfied, leading to the strain compatibility equation as:

$$\frac{1}{Et}\nabla_r^2\nabla_r^2\varphi = -\frac{1}{r}\frac{d}{dr}\left[\frac{1}{2}\left(\frac{dw}{dr}\right)^2\right]. \tag{2.2}$$

To solve Eqs. (2.1) and (2.2), a total of seven boundary conditions are required since Eq. (2.2) can usually be integrated once. Clearly, at infinity, the thin film returns to its initial state, unaffected by the indentation. Therefore, we have far-field boundary conditions as:

$$w, \frac{dw}{dr} \to 0 \quad \text{and} \quad \varphi \to \frac{1}{2}\gamma r^2 \quad \text{as} \quad r \to \infty, \tag{2.3}$$

where γ represents the pre-tension in the sheets, which could arise from residual stress in 2D material systems or surface tension in sheets floating on water (Box et al., 2017; Dai et al., 2020). The boundary conditions at the contact edge $r = a$ need to be determined based on the particular geometry of the indenter.

2.1.2. Winkler's mattress model

The coating problems on elastic half-spaces have been extensively studied (Liu et al., 2019; Box et al., 2020). For our problem involving elastic thin layers and indentation of 2D materials, we will instead exploit the Winkler's mattress model (Winkler, 1867), originating from studies in civil engineering structures. The core concept of this model is that the restoring force is proportional to the local displacement, e.g.

$$q = K_{\text{sub}}w. \tag{2.4}$$

The linearized foundation, with stiffness denoted as K_{sub}, resembles a layer of uncoupled springs, as illustrated in Fig. 2. Physically, this linear foundation model can represent interactions such as a water foundation (Box et al., 2017), a thin (transversely) isotropic compressible elastomer (Dillard et al., 2018; Li et al., 2024b; Li and Dai, 2025), or linearized vdW forces (Zhang and Witten, 2007; Ares et al., 2021; Dai et al., 2022).

2.2. Nondimensionalization

We then introduce the dimensionless variables that will be used throughout the paper. Although the characteristic scale w_* in the vertical direction is not clear at this moment, the horizontal length scale can be described by the Winkler length (Dillard et al., 2018):

$$\ell_* = (B/K_{\text{sub}})^{1/4}. \tag{2.5}$$

The following nondimensionalization is then applied:

$$W = \frac{w}{w_*}, \ R = \frac{r}{\ell_*}, \ \Phi = \frac{\varphi}{B}, \ \mathcal{F} = \frac{F\ell_*^2}{Bw_*}, \ \tau = \frac{\gamma\ell_*^2}{B}, \ \eta = \frac{a}{\ell_*}. \tag{2.6}$$

The governing equations outside the contact region $R \geq \eta$ then become:

$$\frac{1}{R}\frac{d}{dR}\left\{R\frac{d}{dR}\left[\frac{1}{R}\frac{d}{dR}\left(R\frac{dW}{dR}\right)\right]\right\} - \frac{1}{R}\frac{d}{dR}\left(\frac{d\Phi}{dR}\frac{dW}{dR}\right) + W = 0 \tag{2.7}$$

and

$$R\frac{d}{dR}\left[\frac{1}{R}\frac{d}{dR}\left(R\frac{d\Phi}{dR}\right)\right] + \mathcal{K}\left(\frac{dW}{dR}\right)^2 = 0, \tag{2.8}$$

subject to far-field conditions:

$$W(R) \to 0, \quad W'(R) \to 0, \quad \text{and} \quad \Phi(R) \to \tau R^2/2, \quad \text{as} \quad R \to \infty. \tag{2.9}$$

As a result, the only physical parameter in this problem is given by the Föppl–von Kármán number (Blees et al., 2015)

$$\mathcal{K} = Etw_*^2/2B, \tag{2.10}$$

which quantifies the relative rigidity of bending compared to stretching in the sheet. A higher $\mathcal{K}$ indicates that the sheet bends more readily than it stretches, and vice versa. $\mathcal{K}$ appears only in the compatibility equation, suggesting that it has minimal influence for small deflections. It is worth noting that under prescribed indentation depth d, the indentation force becomes part of the solution. For point indentation, indentation force can be easily calculated via the shear force balance around $R = 0$, i.e.,

$$\mathcal{F} = -2\pi \lim_{R\to 0} R\frac{d}{dR}\left[\frac{1}{R}\frac{d}{dR}\left(R\frac{dW}{dR}\right)\right]. \tag{2.11}$$

We use standard boundary value problem solvers, such as `bvp4c` in MATLAB, to solve the problem specified in Eqs. (2.7) to (2.11). In the following text, we refer to these computed results as the "numerical solutions".

2.3. The solution of Box et al. (2017)

Eqs. (2.7) to (2.11) can be used to describe the problem of point indentation of an elastic sheet floating on a water surface, which has been analytically solved for small indentation depths by Box et al. (2017). Below, we briefly outline this solution. For point loading ($\eta = 0$), the inner boundary condition is:

$$W(0) = -\delta, \ W'(0) = 0, \ u(0) = \lim_{R\to 0}\left[\Phi''(R) - \nu\frac{\Phi'(R)}{R}\right] = 0, \ \Phi(0) = 0, \tag{2.12}$$

where $\delta = d/w_*$ is the prescribed indentation depth, $u(r)$ represents the radial displacement field within the sheet, and the value of Φ at $r = 0$ could be arbitrary (since only its derivative is physically meaningful). When the indentation depth is small, Box et al. (2017) considered a linear perturbation for the Airy stress function of the original pretensioned $\Phi = \tau R^2/2 + \bar{\Phi}$ with $|\bar{\Phi}| \ll \tau R^2$. The leading-order term of Eqs. (2.7) and (2.8) reads

$$\nabla_R^4 W - \tau\nabla_R^2 W + W = 0. \tag{2.13}$$

with boundary conditions in Eqs. (2.9) and (2.12), the solution to Eq. (2.13) was obtained:

$$W = -\frac{2\delta}{\ln\left(\lambda_-/\lambda_+\right)}\left[K_0\left(\lambda_+^{1/2}R\right) - K_0\left(\lambda_-^{1/2}R\right)\right], \tag{2.14}$$

where $K_n(r)$ is the modified Bessel function of nth order and $\lambda_\pm = (\tau \pm \sqrt{\tau^2 - 4})/2$. The indentation force could be calculated with Eq. (2.11), leading to a indentation stiffness:

$$K_p = \frac{F}{\delta} = 2\pi\frac{(\tau^2 - 4)^{1/2}}{\text{arc tanh}\left[\left(1 - 4/\tau^2\right)^{1/2}\right]} \sim \begin{cases} 8, & \tau \ll 1 \\ 2\pi\tau/\ln\tau, & \tau \gg 1 \end{cases}, \tag{2.15}$$

which is Eq.(4.13) in Box et al. (2017).

2.4. Implications and extensions

Interestingly, Eq. (2.13) can also describe the indentation problem of a plate on a Pasternak foundation (Kerr, 1964), where the restoring force of substrate is given by

$$q(w) = K_{\text{sub}}w - G_p\nabla^2 w, \tag{2.16}$$

with K_{sub} and G_p determined by the elastic modulus and thickness of the substrate (Argatov et al., 2015). In this context, τ in Eq. (2.6) should be redefined as $(\gamma + G_p)/\ell_*^2 B$, in which the term involving G_p can be used to account for the deviatoric deformation in the substrate—a crucial factor when the substrate becomes incompressible (Dillard et al., 2018; Chandler and Vella, 2020b; Hao et al., 2024). In other words, by appropriately modifying the pre-tension, the indentation model and analytical approach based on the Winkler foundation can also be applied to higher-order substrate theories, thereby enhancing the versatility of the model.
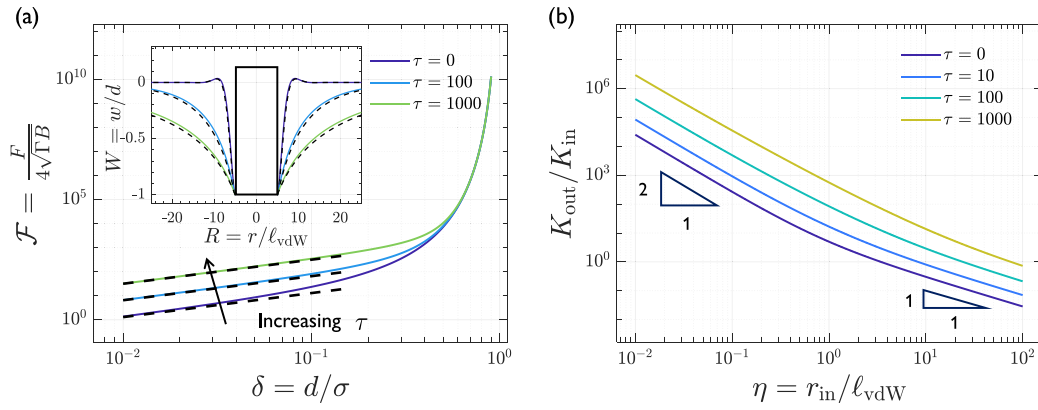
Fig. 3. (a) Dimensionless indentation force–depth curve of punch indentation (the dimensionless punch radius $\eta = 5$) on a van der Waals foundation. The inset shows the normalized deformation profile of the thin sheet (calculated at $\delta = 0.01$). (b) The ratio of two stiffness components K_{out}/K_{in} (see the definition in Eqs. (3.10) and (3.11)) as a function of the dimensionless indenter radius. Since $K_{in} \propto \eta^2$, the transition in scaling behavior indicates that K_{out} changes from independent of the indenter radius to linearly dependent on it.

In addition to small indentation depths, a key assumption for the validity of Eq. (2.15) is that the indenter size, r_{in}, must be much smaller than the characteristic horizontal length, ℓ_*. However, as demonstrated in the experiments reported in Gao et al. (2015, 2018), Cellini et al. (2018), Mandriota et al. (2019), the ratio r_{in}/ℓ_* can reach up to $O(10)$, making the effect of both the size and shape of the indenter significant. Additionally, pre-tension introduces an additional length scale (alongside the Winkler-type length), further complicating the influence of indenter size and shape. In the rest of this paper, we address these complexities and discuss the conditions under which the system can be effectively linearized.

3. Punch indentation with van der Waals foundations

In this section, we discuss the problem of punch indentation based on linearized van der Waals interactions with the substrate. In this problem, the contact area is known and does not vary with the indentation depth, which is also known as "conformal contact" (Barber, 2018). This allows us to focus on the asymptotic behavior and physical implications of the solutions.

3.1. Van der Waals foundation

Inspired by indentation experiments where 2D material sheets adhere to a rigid substrate through van der Waals forces (Gao et al., 2015, 2018; Cellini et al., 2018), we extend the linear foundation in Eq. (2.7) to incorporate the lateral force q in (2.1) contributed by nonlinear vdW interactions. Specifically, by integrating the intermolecular Lennard-Jones potential, the vdW interaction can be written as a function of the film deflection (Israelachvili, 2011):

$$q(w) = \frac{8\Gamma}{3\sigma}\left[\frac{1}{(w/\sigma + 1)^3} - \frac{1}{(w/\sigma + 1)^9}\right], \tag{3.1}$$

where Γ is the adhesion energy and σ is the equilibrium separation between the sheet and the substrate (Yu et al., 2025). Note that under small deflections, the linearization of Eq. (3.1) yields a Winkler foundation response:

$$q = K_{vdW}w \quad \text{and} \quad K_{vdW} = \left.\frac{dq}{dw}\right|_{w=0} = \frac{16\Gamma}{\sigma^2}. \tag{3.2}$$

Similar equivalent stiffness of vdW interactions has also been used in studies of winkling instabilities (Zhang and Witten, 2007; Davidovitch and Guinea, 2021; Ares et al., 2021; Dai et al., 2022), and graphene blistering under small deflections (Wang et al., 2016). Thus, in the context of vdW foundation, the rescaling process discussed in Section 2.2

can be simply proceeded by updating the K_{sub} with K_{vdW} given in Eq. (3.2) and replacing w_* with σ:

$$W = \frac{w}{\sigma}, \ \delta = \frac{d}{\sigma}, \ R = \frac{r}{\ell_{vdW}}, \ \Phi = \frac{\varphi}{B}, \ \mathcal{F} = \frac{F}{4\sqrt{\Gamma B}},$$

$$\tau = \frac{\gamma\sigma}{4\sqrt{\Gamma B}}, \ \ell_* = \ell_{vdW} = \left(\frac{B\sigma^2}{16\Gamma}\right)^{1/4}, \ \mathcal{K} = \frac{Et\sigma^2}{2B}. \tag{3.3}$$

Now the compatibility Eq. (2.8) holds while the equilibrium equations becomes

$$\frac{1}{R}\frac{d}{dR}\left\{R\frac{d}{dR}\left[\frac{1}{R}\frac{d}{dR}\left(R\frac{dW}{dR}\right)\right]\right\} - \frac{1}{R}\frac{d}{dR}\left(\frac{d\Phi}{dR}\frac{dW}{dR}\right)$$
$$+ \frac{1}{6}\left[\frac{1}{(W+1)^3} - \frac{1}{(W+1)^9}\right] = 0. \tag{3.4}$$

It may be worth noting that for monolayer 2D materials, $\mathcal{K}$ can be extremely large, ranging from 100 to 1000 as they resist stretching by the strong in-plane covalent bonds and bending by a different physical origin, i.e., weak out-of-plane π bonds (Wang et al., 2019; Dai and Lu, 2021).

3.2. Punch indentation

We now consider a punch indentation as illustrated in Fig. 2. The far-field boundary conditions in Eq. (2.9) remain applicable, while the inner boundary conditions at the periphery of the indenter (i.e., at $R = \eta = r_{in}/\ell_{vdW}$) are given by

$$W(\eta) = -\delta, \quad W'(\eta) = 0, \quad \Phi''(\eta) - \nu\frac{\Phi'(\eta)}{\eta} = (1-\nu)\tau, \quad \Phi(0) = 0, \tag{3.5}$$

In Eq. (3.5), the third equation specifies that the radial displacement at $R = \eta$ is purely caused by pre-tension before indentation, corresponding to a no-slip indenter tip. In fact, even a perfect-slip indenter has no impact on the indentation stiffness at small indentation depths, as the linearized governing equation can be solved using only the boundary conditions related to W. The numerical solutions to Eqs. (3.4) and (2.8) subject to Eqs. (3.5) and (2.9) for $\eta = 5$ and various pre-tension τ are presented as solid curves in Fig. 3.

At small indentation depths, the linearization of Eq. (3.4) still gives rise to Eq. (2.13). We solve this analytically with boundary conditions (2.9) and (3.5), obtaining the deformation profile of the sheet undergoing punch indentation:

$$W(R) = C_1 K_0\left(\lambda_+^{1/2}R\right) + C_2 K_0\left(\lambda_-^{1/2}R\right), \tag{3.6}$$

In Eq. (3.6), C_1 and C_2 are constants that can be determined by boundary conditions (3.5). Specifically,

$$C_1 = \frac{K_{1-}\lambda_-^{1/2}\delta}{K_{0-}K_{1+}\lambda_+^{1/2} - K_{0+}K_{1-}\lambda_-^{1/2}}, \quad \text{and}$$

$$\tag{3.7}$$

$$C_2 = \frac{K_{1+}\lambda_+^{1/2}\delta}{K_{0+}K_{1-}\lambda_-^{1/2} - K_{0-}K_{1+}\lambda_+^{1/2}},$$

here $K_{0+} = K_0\left(\lambda_+^{1/2}\eta\right), K_{0-} = K_0\left(\lambda_-^{1/2}\eta\right), K_{1+} = K_1\left(\lambda_+^{1/2}\eta\right), K_{1-} = K_1\left(\lambda_-^{1/2}\eta\right)$. We can then calculate the indentation force by integrating the restoring force of the entire substrate:

$$\mathcal{F} = \mathcal{F}_{\text{in}} + \mathcal{F}_{\text{out}}, \tag{3.8}$$

where the net force underneath the indenter reads $\mathcal{F}_{\text{in}} = 2\pi \int_0^\eta \delta R\, dR$, and the net force outside of the contact region reads $\mathcal{F}_{\text{out}} = -2\pi \int_\eta^\infty W(R)R\, dR$. Obviously, such an integration reveals a linear force–displacement relationship (since C_1 and C_2 are linearly proportional to δ). We then have the corresponding indentation stiffness contributed by two regions:

$$K = K_{\text{out}} + K_{\text{in}}, \tag{3.9}$$

Obviously, the stiffness due to the compression of the vdW foundation underneath the punch is given by

$$K_{\text{in}} = \pi\eta^2, \tag{3.10}$$

and the stiffness due to the deflection of the sheet outside of the contact region is given by

$$K_{\text{out}} = -2\pi\eta\left(C_1\lambda_+^{-1/2}K_{1+} + C_2\lambda_-^{-1/2}K_{1-}\right)/\delta. \tag{3.11}$$

Fig. 3a shows the comparison between analytical (dashed curves) and numerical (solid curves) results regarding the deformed profile of the sheet and the indentation force–depth relation. The color of solid curves represents different values of pre-tension. It is clear that the linearized equations (3.6) and (3.8) effectively capture the mechanical behavior of the system at small indentation depths (i.e., $\delta \ll 1$). Fig. 3b shows the relationship between $K_{\text{out}}/K_{\text{in}}$ (as defined in Eqs. (3.10) and (3.11)) and the dimensionless indenter radius η across different levels of pre-tensions. Interestingly, at small pre-tensions, the following transition can be observed with the increase of the dimensionless indenter size:

$$K_{\text{out}}/K_{\text{in}} \sim \eta^{-2} \quad \rightarrow \quad K_{\text{out}}/K_{\text{in}} \sim \eta^{-1}. \tag{3.12}$$

However, this transition is hardly observed at large pre-tensions, suggesting that the effects of pre-tension and indenter size are indeed coupled. We therefore turn to clarify the dependence of the indentation stiffness on the indenter size and pre-tension via a regime diagram.

3.3. A regime diagram

We then attempt to provide the parametric phase diagram illustrating the effects of the indenter radius and pre-tension on indentation stiffness. This task is complicated by the characteristic lengths of the system that can be eventually changed by pre-tension.

3.3.1. Horizontal length scales

The complex dependence of the indentation stiffness on indenter size and pre-tension in Fig. 3b suggests that additional length scales, beyond ℓ_{vdW} in Eq. (3.3), may be influential. To examine this further, we revisit the dimensional form of the linearized equation (3.4):

$$B\nabla_r^4 w - \gamma\nabla_r^2 w + K_{\text{vdW}}w = 0, \tag{3.13}$$

where the three terms on the LHS correspond to the bending term, pre-tension term, and term of the substrate restored force, respectively. From Eq. (3.13), we naturally consider three limiting regimes:

(*i*) Bending-dominated regime. Comparing the first and third terms ($B/\ell_B^4 \sim K_{\text{vdW}}$), we obtain a "bending characteristic length" of a plate on a Winker foundation: $\ell_B = (B/K_{\text{vdW}})^{1/4}$ (which is ℓ_{vdW} we have been using in the preceding discussion). (*ii*) Pretension-dominated regime. Comparing the second and third terms ($\gamma/\ell_\gamma^2 \sim K_{\text{vdW}}$), we obtain a "pre-tension characteristic length" of the system: $\ell_\gamma = (\gamma/K_{\text{vdW}})^{1/2}$. (*iii*) Regime of comparable bending and pre-tension effect. Comparing the first two terms, we obtain a "bending-pretension characteristic length": $\ell_{B\gamma} = (B/\gamma)^{1/2}$, which also balances the bending energy and stretching energy due to pre-tension. These three characteristic lengths describe the competition between three distinct physical ingredients. We now analyze their relative importance in different positions and how they relate to the indentation stiffness.

As shown in Fig. 2 and the inset of Fig. 3a, the indentation profile of the sheet can be roughly divided into two regions with opposite curvatures. (a) In the area close to the indenter, there is a boundary layer with upward curvature due to the finite bending stiffness of the elastic sheet. We denote the horizontal length of this "boundary layer" as ℓ_{in}, and the vertical length as d_{in}. (b) In the area outside the boundary layer (hereinafter referred to as the "outer annulus"), the curvature of the film turns downward. We denote the horizontal length of the outer annulus as ℓ_{out}, and its vertical length as d_{out}. For small indentation depth, we assume that the two parts have self-similar shapes, allowing us to relate the characteristic scales in the horizontal and vertical directions via

$$d_{\text{in}} = \frac{\ell_{\text{in}}}{\ell_{\text{in}} + \ell_{\text{out}}}d, \quad \text{and} \quad d_{\text{out}} = \frac{\ell_{\text{out}}}{\ell_{\text{in}} + \ell_{\text{out}}}d. \tag{3.14}$$

When there is no pre-tension: $\ell_{\text{in}} \sim \ell_{\text{out}} \sim \ell_B$. As pre-tension increases, the influence of bending diminishes, though at different rates in the boundary layer and outer annulus. For instance, in the limiting case of very high pre-tension, the bending stiffness in the outer annulus can be considered negligible, while bending remains significant within the boundary layer. Thus, when estimating the characteristic length scale, the interaction between bending stiffness and pre-tension must be consistently considered. This leads to the selection of the characteristic lengths as follows:

$$\ell_{\text{in}} \sim \min\left\{\ell_{B\gamma}, \ell_B\right\} \quad \text{and} \quad \ell_{\text{out}} \sim \max\left\{\ell_\gamma, \ell_B\right\} \tag{3.15}$$

3.3.2. Small pre-tensions ($\tau \ll 1$)

When the dimensionless pre-tension τ is small ($\tau \ll 1$), its dimensional form reads $\gamma \ll \sqrt{BK_{\text{vdW}}}$. This reveals the magnitudes of the three characteristic lengths discussed in Section 3.3.1:

$$\ell_\gamma \ll \ell_B \ll \ell_{B\gamma}. \tag{3.16}$$

According to Eqs. (3.14) and (3.15), we have:

$$\ell_{\text{in}} \sim \ell_{\text{out}} \sim \ell_B \quad \text{and} \quad d_{\text{in}} \sim d_{\text{out}} \sim d. \tag{3.17}$$

Eq. (3.17) suggests a bending-dominated indentation behavior, enabling us to analyze k_{out} (dimensional form of K_{out} defined in (3.11)) from an energy perspective. In particular, when the indenter radius is much smaller than the characteristic scale of the system (i.e., $r_{\text{in}} \ll \ell_B$), the balance between the work done by the external force and the stored strain energy gives:

$$k_{\text{out}}d^2 \sim \ell_{\text{in}}^2 B\left(\frac{d_{\text{in}}}{\ell_{\text{in}}^2}\right)^2 + \ell_{\text{out}}^2 B\left(\frac{d_{\text{out}}}{\ell_{\text{out}}^2}\right)^2 \sim \sqrt{BK_{\text{vdW}}}d^2, \tag{3.18}$$

where d/ℓ^2 is the characteristic curvature κ of the sheet, and ℓ_{in}^2 and ℓ_{out}^2 represent the estimation of the area of the boundary layer and outer annulus, respectively. Eq. (3.18) also tells us $K_{\text{out}} \sim 1$, independent of indenter radius and pre-tension. Note that this conclusion can also be drawn by considering the energy stored in the foundation scaling as $K_{\text{vdW}}\ell_B^2 d^2 \sim \sqrt{BK_{\text{vdW}}}d^2$.
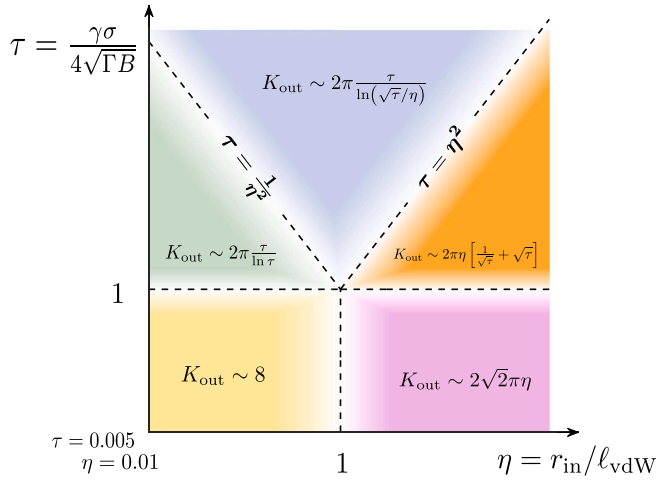
Fig. 4. The outer stiffness K_{out} in the parameter regime (dimensionless pre-tension τ, dimensionless indenter radius η). The colored areas reveal different asymptotic behaviors of K_{out}, and the light area represents the transition area that has been numerically verified, where the asymptotic results may exhibit some inaccuracies.

In contrast, when $r_{\text{in}} \gg \ell_B$, the sizes of the boundary layer and outer annulus should be re-examined:

$$k_{\text{out}} d^2 \sim r_{\text{in}} \ell_{\text{in}} B \left(\frac{d_{\text{in}}}{\ell_{\text{in}}^2} \right)^2 + r_{\text{in}} \ell_{\text{out}} B \left(\frac{d_{\text{out}}}{\ell_{\text{out}}^2} \right)^2 \sim r_{\text{in}} B^{1/4} K_{\text{vdW}}^{3/4} d^2, \quad (3.19)$$

which suggests $K_{\text{out}} \sim \eta$. As a reference, we rigorously deduced the asymptotic behaviors of K_{out} based on Eq. (3.11), which indeed gives:

$$K_{\text{out}} \sim \begin{cases} 8, & \text{for } \eta \ll 1 \\ 2\sqrt{2}\pi\eta, & \text{for } \eta \gg 1 \end{cases}, \quad (3.20)$$

which is further illustrated in the regime diagram in Fig. 4 (i.e., the two blocks on the bottom).

3.3.3. Large pre-tensions ($\tau \gg 1$)

Similarly, when the elastic sheet undergoes a large pre-tension: $\tau \gg 1$ (i.e., $\gamma \gg \sqrt{BK_{\text{vdW}}}$), the three characteristic scales show the reverse order:

$$\ell_\gamma \gg \ell_B \gg \ell_{B\gamma}, \quad (3.21)$$

which leads to an estimation according to Eqs. (3.14) and (3.15):

$$\ell_{\text{in}} \sim \ell_{B\gamma}, \quad \ell_{\text{out}} \sim \ell_\gamma, \quad d_{\text{in}} \sim \frac{\ell_{B\gamma}}{\ell_\gamma} d, \quad d_{\text{out}} \sim d. \quad (3.22)$$

In this case, the energy contributions from bending and pre-tension are comparable in the boundary layer, while the energy due to pre-tension dominates over the bending energy in the outer annulus. Therefore, when the radius of the indenter is much smaller than the minimum characteristic length of the system (i.e., $r_{\text{in}} \ll \ell_{B\gamma}$ or $\tau \ll \eta^{-2}$ in dimensionless form), we can estimate k_{out} by considering

$$k_{\text{out}} d^2 \sim \ell_{\text{in}}^2 \gamma \frac{d_{\text{in}}^2}{\ell_{\text{in}}^2} + \ell_{\text{out}}^2 \gamma \frac{d_{\text{out}}^2}{\ell_{\text{out}}^2} \sim \left[1 + \left(\frac{\ell_{B\gamma}}{\ell_\gamma} \right)^2 \right] \gamma d^2, \quad (3.23)$$

where $(d/\ell)^2$ is the indentation-induced strain in the sheet. Ignoring the effect of the boundary layer (as its effect has become secondary), we obtain $K_{\text{out}} \sim \tau$. When the radius of the indenter is much greater than the maximum characteristic length of the system (i.e., $r_{\text{in}} \gg \ell_\gamma$ or $\tau \gg \eta^2$), we instead have

$$k_{\text{out}} d^2 \sim r_{\text{in}} \ell_{\text{in}} \gamma \frac{d_{\text{in}}^2}{\ell_{\text{in}}^2} + r_{\text{in}} \ell_{\text{out}} \gamma \frac{d_{\text{out}}^2}{\ell_{\text{out}}^2} \sim \frac{r_{\text{in}} \gamma}{\ell_\gamma} \left(1 + \frac{\ell_{B\gamma}}{\ell_\gamma} \right) d^2, \quad (3.24)$$

which implies $K_{\text{out}} \sim \eta \left[\sqrt{\tau} + 1/\sqrt{\tau} \right]$. Similarly, using the properties of the Bessel function, we can obtain the asymptotic solution of Eq. (3.11) under large pre-tensions:

$$K_{\text{out}} \sim \begin{cases} 2\pi \dfrac{\tau}{\ln \tau}, & \text{for } \eta \ll \tau^{-1/2} \\[2mm] 2\pi \dfrac{\tau}{\ln\left(\sqrt{\tau}/\eta\right)}, & \text{for } \tau^{-1/2} \ll \eta \ll \tau^{1/2} \\[2mm] 2\pi\eta \left[\dfrac{1}{\sqrt{\tau}} + \sqrt{\tau} \right], & \text{for } \eta \gg \tau^{1/2}, \end{cases} \quad (3.25)$$

which is shown in the regime diagram in Fig. 4 (see the top three blocks).

3.3.4. A summary of τ and η dependence

The diagram in Fig. 4 divides the (η, τ) space into five regimes, illustrating the asymptotic expressions of K_{out} under different parameter combinations. To further verify this regime diagram, we show in Fig. 5a the evolution of K_{out} as a function of pre-tension τ with different indenter radius η. With small indenter radii ($\eta \ll 1$), as the pre-tension increases, the outer stiffness initially exhibits an asymptotic behavior that is nearly identical to that of a point indenter. With further increases in pre-tension, the influence of the indenter size η will eventually manifest through a logarithmic correction. With large indenter radii, as the pretension increases, the external stiffness approximately exhibits the following scaling transitions: $K_{\text{out}} \sim \tau^0 \to \tau^{1/2} \to \tau$. Fig. 5b further shows the evolution of K_{out} as a function of the indenter radius η with different pre-tension τ. At small pre-tensions, with the increase in indenter radius, the outer stiffness undergoes a transition from being independent of η to finally linearly dependent on η, regardless of the pre-tension level. However, at large pre-tensions, there exists an intermediate regime where the stiffness logarithmically depends on the indenter radius. The "size" of this intermediate regime expands with increasing pre-tension. This explains the power-law transition observed in Fig. 3b and why this transition is hardly seen at large pre-tensions.

In summary, when $\tau \ll 1$, the effect of pretension on the indentation stiffness can be safely ignored; however, careful consideration of the indenter radius is necessary unless $r_{\text{in}}/\ell_B \ll \min\left\{\tau^{-1/2}, 1\right\}$. In typical 2D material experiments (such as in Gao et al., 2015, 2018; Cellini et al., 2018), we may take $\sigma = 0.6$ nm, $\Gamma = 0.1$ J/m^2, $B = 1.5$ eV (Wang et al., 2016). Under these conditions, $\ell_B \approx 0.48$ nm (indicating a significant effect of indenter size for probes only a few nanometers large), and the corresponding pre-tension for $\tau^{-1/2} \sim 1$ is $\gamma \approx 1.03$ N/m.
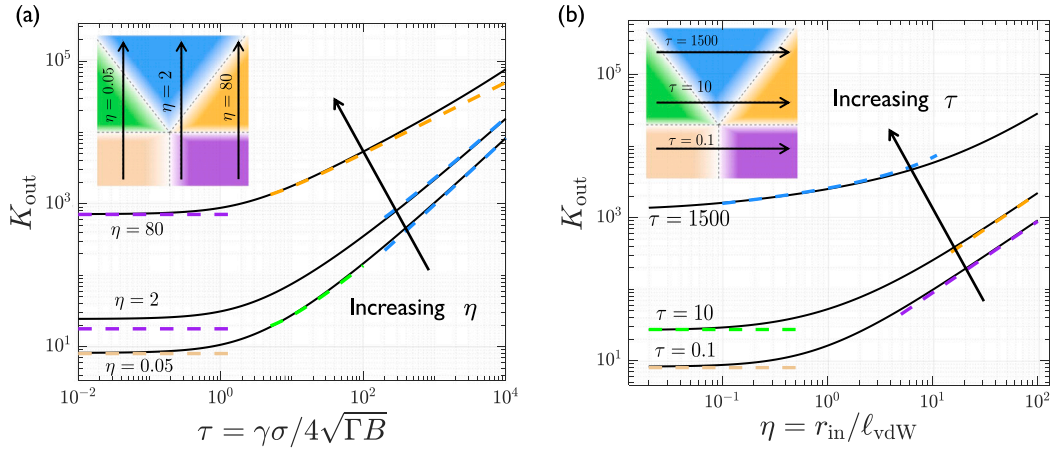
3.4. Nonlinearities

The indentation stiffness for cylindrical indenters is derived above using the linearized Eq. (2.13). These results significantly simplify the interpretation of experimental data, facilitating the extraction of material and foundation properties. However, it is essential to clearly define its applicability to avoid potential pitfalls.

We first examine the emergence of geometric nonlinearity due to indentation-induced strain in the sheet, again from an energy perspective (Chen and Dai, 2023; Dai, 2024). When $\tau \ll 1$ (i.e., in the bending-dominated regime), the strain energy in the boundary layer and the outer annulus are comparable. For the bending energy to be comparable to the induced stretching energy, the indentation depth must satisfy:
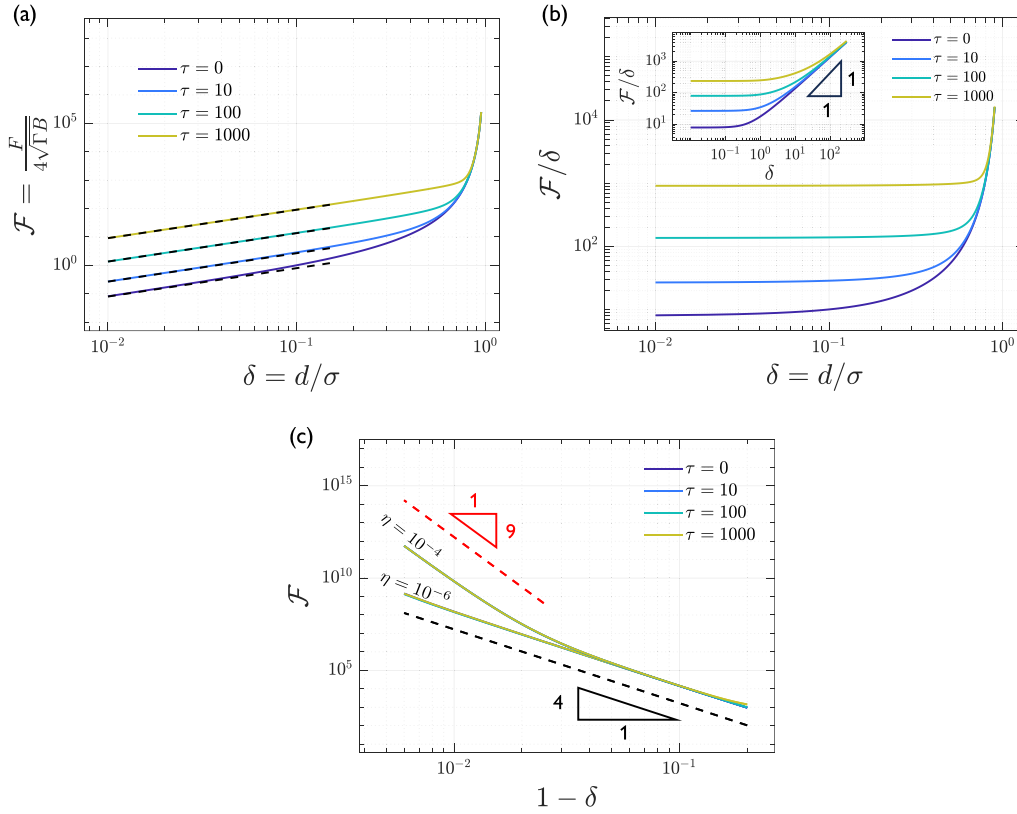
$$B \left(\frac{d}{\ell_B^2} \right)^2 \sim Et \left(\frac{d}{\ell_B} \right)^4 \quad \Rightarrow \quad d_c \sim (B/E_{2D})^{1/2}. \quad (3.26)$$

The corresponding dimensionless depth is thus $\delta_c \sim \mathcal{K}^{-1/2}$. When $\tau \gg 1$ (i.e., in the pretension-dominated regime), the energy in the boundary layer is proportional to that in the outer annulus (as shown in Eqs. (3.23) and (3.24)). Considering only the energy balance in the outer annulus, we obtain

$$\gamma \left(\frac{d}{\ell_\gamma} \right)^2 \sim Et \left(\frac{d}{\ell_\gamma} \right)^4 \quad \Rightarrow \quad d_c \sim \left(\frac{\gamma^2}{K_{\text{sub}} E_{2D}} \right)^{1/2}, \quad (3.27)$$

Fig. 5. (a) The evolution of outer stiffness K_{out} as a function of pre-tension τ with different indenter radius η. (b) The evolution of outer stiffness K_{out} as a function of indenter radius η with different pre-tension τ. The black solid curves represent the complete indentation stiffness expression given in Eq. (3.11), and the dashed curves of different colors represent the asymptotic expressions reflected in the corresponding parameter regime in the inset.

Fig. 6. (a) Indentation force–depth relationship of point loading with nonlinear van der Waals foundation. (b) Apparent stiffness $\mathcal{F}/\delta$ as a function of indentation depth. The flat portion of the curve with zero slope corresponds to a linear force–displacement relationship. The inset shows the $\mathcal{F}/\delta \sim \delta$ curves with linearized foundation. (c) $\mathcal{F} \sim 1 - \delta$ curves for $\eta = 10^{-4}$ and $\eta = 10^{-6}$ when $\delta > 0.8$. The dashed lines represent the scaling relation in Eq. (3.32). Here the force–displacement curves for different pre-tensions lie on top of each other.

and hence the corresponding dimensionless depth $\delta_c \sim \tau \mathcal{K}^{-1/2}$. Therefore, due to the geometrical nonlinearity in the elastic sheet, the premise for the linearized theory to hold is $\delta \ll \delta_c$.

In Fig. 6a, we use a point indenter ($\mathcal{K} = 100$) to show the indentation force–depth curve with a nonlinear vdW foundation. The linear regime is reflected in the flat portion of the $\mathcal{F}/\delta - \delta$ plot in Fig. 6b. To get rid of the nonlinearity due to the foundation, the inset in Fig. 6b provides the relationship between the apparent indentation stiffness $\mathcal{F}/\delta$ and indentation depth δ for a linearized vdW substrate under identical conditions, which validates the prediction of Eqs. (3.26) and (3.27). In addition, at large indentation depth, indentation on the linear

foundation exhibits an $\mathcal{F} \sim \delta^2$ relationship (which has also been discussed in Box et al. (2017)).

For the nonlinear vdW foundation, however, the singularity requires extra considerations. As the dimensionless indentation depth δ approaches 1, the short-range repulsive force of the van der Waals substrate beneath the indenter gradually becomes $(1 - \delta)^{-9}$ singular. As a result, even though the scale of the bending boundary layer is small, the high intensity of the distributed force can still exert a non-negligible influence on the indentation force. We denote the horizontal scale of the bending boundary layer as ℓ_s, which cannot be simply estimated using the three characteristic lengths from Section 3.3.1 due
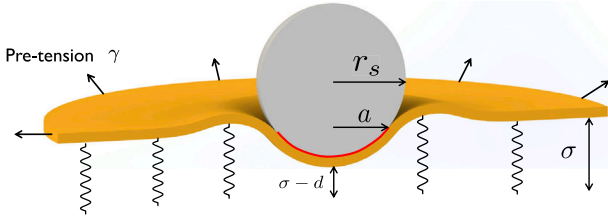
Fig. 7. Schematic illustration of the spherical indentation model, where a spherical indenter of radius r_s makes contact with the thin film, forming a contact area of unknown radius a. At small indentation depths, the shape of the spherical indenter can be approximated as a paraboloid according to Derjaguin et al. (1975).

to strong nonlinearity. Meanwhile, the vertical scale δ_s of the boundary layer, which is crucial for estimating the bending energy, also need to be determined. This is because the simple self-similar approximation (Eq. (3.14)) no longer holds when the vdW singularity has a significant effect only within the boundary layer.

To determine the horizontal scale ℓ_s and vertical scale δ_s of the boundary layer, two relationships are required. The first relationship is derived from an energy perspective: The dimensionless bending energy within the boundary layer and the energy stored in the substrate beneath are given by:

$$\mathcal{U}_{\text{bend}} \sim \ell_s^2 \left(\frac{\delta_s}{\ell_s^2} \right)^2 \sim \frac{\delta_s^2}{\ell_s^2} \quad \text{and} \quad \mathcal{U}_{\text{sub}} \sim \ell_s^2 (1-\delta)^{-8}, \tag{3.28}$$

respectively. Minimizing the sum of these two dominant energy contributions yields $\delta_s \sim \ell_s^2 (1-\delta)^{-4}$. It is worth noting that the choice of characteristic area does not affect the energy minimization result; therefore, the relative size of the indenter radius and ℓ_s does not need to be considered. The second relationship is derived from a geometric perspective. Considering the bending term and the substrate repulsive force term in Eq. (3.4) (since these two are the most critical for boundary layer), we have:

$$\frac{\delta_s}{\ell_s^4} \sim \frac{1}{(1-\delta)^9}. \tag{3.29}$$

Solving Eqs. (3.28) and (3.29), we have

$$\delta_s \sim 1 - \delta \quad \text{and} \quad \ell_s \sim (1-\delta)^{5/2}. \tag{3.30}$$

Following a similar discussion on characteristic areas as in Section 3.3, we obtain the singular substrate energy in the two limiting cases of different indenter radii:

$$\mathcal{U}_{total} \sim \begin{cases} \ell_s^2 (1-\delta)^{-8} \sim (1-\delta)^{-3}, & \text{for } \eta \ll (1-\delta)^{5/2} \ll 1 \\ \eta^2 (1-\delta)^{-8} \sim (1-\delta)^{-8}, & \text{for } (1-\delta)^{5/2} \ll \eta \ll 1, \end{cases} \tag{3.31}$$

which yield the indentation force:

$$\mathcal{F} \sim \begin{cases} (1-\delta)^{-4}, & \text{for } \eta \ll (1-\delta)^{5/2} \ll 1 \\ (1-\delta)^{-9}, & \text{for } (1-\delta)^{5/2} \ll \eta \ll 1. \end{cases} \tag{3.32}$$

This means that in the limit of an extremely small indenter, even when the indentation depth is close to 1, the presence of bending stiffness prevents the $(1-\delta)^{-9}$ singularity predicted by the vdW interaction. This is because the transverse scale of the singular region also depends on the indentation depth δ. In Fig. 6c, we show this scaling relation together with numerics obtained under two different indenter radii.

4. Spherical indentation with linear foundations

In the previous section, we have revealed a linear punch indentation response for thin sheets on vdW foundations when the indentation depth is small and the vdW foundation can hence be linearized. In

this section, we apply the same vdW foundation to a spherical indenter, which may better reflect the conditions of actual indentation experiments performed on cells and 2D materials (Mandriota et al., 2019; Cellini et al., 2018). As shown in Fig. 7, we consider a spherical indenter with radius r_s, which forms a contact area with radius a when the indentation depth, defined as the downward distance between the bottom of the sphere and the equilibrium position of the film, is d. The key difference between a spherical indenter and a cylindrical indenter is that as the indentation depth increases, the contact area between the indenter and the thin film also increases, leading to a movable boundary. Accordingly, we give the dimensionless contact radius and sphere radius as

$$\eta = \frac{a}{\ell_{\text{vdW}}} \quad \text{and} \quad R_s = \frac{r_s}{r_c}, \tag{4.1}$$

respectively, where $r_c = \ell_{\text{vdW}}^2 / 2\sigma$ is a typical radius. The definitions of ℓ_{vdW} and σ can be found in Eq. (3.3).

4.1. Boundary conditions

We use the same Eqs. (3.4) and (2.8), but new indenter geometry requires redefining the boundary conditions at the contact line ($R = \eta$) as follows:

$$W(\eta) = -\delta + \frac{\eta^2}{R_s}, \quad W'(\eta) = \frac{2\eta}{R_s}, \quad W''(\eta) = \frac{2}{R_s},$$

$$\Phi''(\eta) - \frac{\Phi'(\eta)}{\eta} = -\mathcal{K} \frac{\eta^2}{R_s^2}, \quad \Phi(\eta) = 0. \tag{4.2}$$

Here, we have assumed that the sheet fully conforms to the indenter inside the contact region and the indenter shape is approximated by a paraboloid. Therefore, the first equation in (4.2) represents the indentation depth condition. We consider nonvanishing bending stiffness and assume no adhesion between the indenter and the sheet so the slope and curvature continuity conditions at the contact line are ensured by the second and third equations. Substituting the first equation of (4.2) into the compatibility Eq. (2.8) and eliminating the undetermined parameters yields the fourth boundary condition for the Airy stress function Φ. An additional boundary condition, compared to a punch indentation, is required to determine the contact radius η as a function of indentation depth. To facilitate numerical computation, we initially relax the curvature continuity condition and use the remaining four boundary conditions to obtain the solution for a given contact radius and indentation depth. The indentation depth is then iteratively adjusted using the Newton–Raphson method to satisfy the curvature continuity condition. The numerical solutions are presented as solid curves in Fig. 8.

4.2. Analytical results

We then seek analytical solutions to the spherical indentation problem by linearizing Eq. (3.4) to be Eq. (2.13). Solving Eq. (2.13) subjected to boundary conditions (4.2) yields the film deflection curve in the form of Eq. (3.6) with the following values for C_1 and C_2:

$$C_1 = \frac{-2K_{0-}\eta - K_{1-}\lambda_-^{1/2}\eta^2 + \delta K_{1-}\lambda_-^{1/2}R_s}{R_s \left(K_{0-}K_{1+}\lambda_+^{1/2} - K_{0+}K_{1-}\lambda_-^{1/2} \right)} \quad \text{and}$$
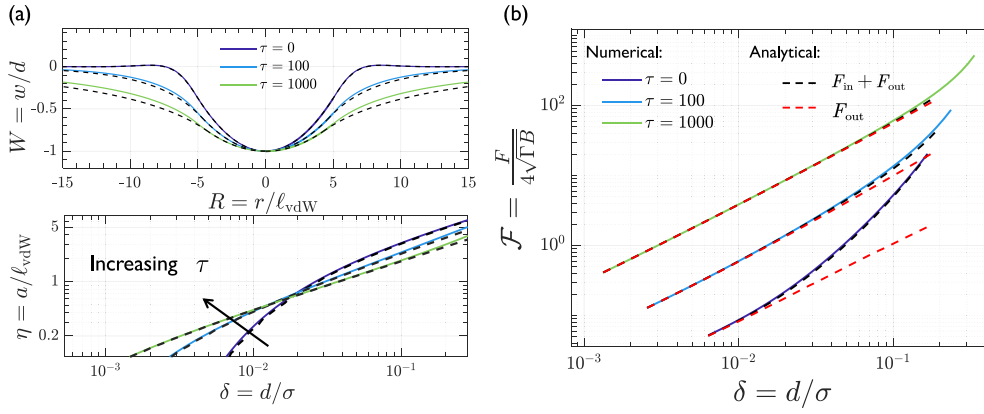
$$C_2 = \frac{2K_{0+}\eta + K_{1+}\lambda_+^{1/2}\eta^2 - \delta K_{1+}\lambda_+^{1/2}R_s}{R_s \left(K_{0-}K_{1+}\lambda_+^{1/2} - K_{0+}K_{1-}\lambda_-^{1/2} \right)} \tag{4.3}$$

with η implicitly given by

$$C_1 \lambda_+ \left(K_{0+} + K_{2+} \right) + C_2 \lambda_- \left(K_{0-} + K_{2-} \right) = 4/R_s, \tag{4.4}$$

where the definition of $K_{n\pm}$ is the same as in Section 3.2. Again, the indentation force can be obtained by combining the repulsive force inside and outside the contact line, say $\mathcal{F} = \mathcal{F}_{\text{in}} + \mathcal{F}_{\text{out}}$, where

$$F_{\text{in}} = -2\pi \int_0^\eta \frac{1}{6} \left[\frac{1}{(W(R)+1)^3} - \frac{1}{(W(R)+1)^9} \right] R \, dR \tag{4.5}$$

Fig. 8. (a) Normalized deflection calculated numerically with $\eta = 2.5$ (top panel) and the evolution of the contact radius as a function of indentation depth (bottom panel) for different pre-tensions. (b) Indentation force–depth curves under different pre-tensions. The solid curves represent numerical solutions; The black dashed curves correspond to the expression combining Eqs. (4.5) and (4.6), while the red dashed curves only show the contribution by the region outside the contact area, i.e., Eq. (4.6). Here $R_s = 50$.

here $W(R) = -\delta + R^2/R_s$ due to indenter geometry and

$$F_{\text{out}} = -2\pi\eta \left(C_1 \lambda_+^{-1/2} K_{1+} + C_2 \lambda_-^{-1/2} K_{1-} \right). \tag{4.6}$$

Fig. 8a shows the normalized deflection (top panel) and the evolution of the contact radius as a function of the indentation depth (bottom panel), both show good agreement between the analytical solution (denoted by dashed curves) and numerical solutions (denoted by solid curves). As expected, the growth rate of the contact radius decreases with the increase of the pre-tension. This leads to the fact that when the dimensionless indentation depth $\delta \lesssim 0.02$, a larger pretension corresponds to a larger contact radius, while the opposite is true when $\delta \gtrsim 0.02$.

Although Eq. (4.4) is highly non-linear, in the limit of small pre-tensions ($\tau \ll 1$) we can still make some analytical progress. In particular, when $\delta R_s \gg C_*$ (C_* will be discussed shortly), Eq. (4.4) is simplified to $\eta^2 + 2\sqrt{2}\eta - \delta R_s + 2 = 0$, so the contact radius is solved as

$$\eta = \sqrt{\delta R_s} - \sqrt{2}. \tag{4.7}$$

Alternatively, when $\delta R_s \ll C_*$, the contact radius turns to be

$$\eta = e^{-\pi/(\delta R_s)}. \tag{4.8}$$

Here, the transition point C_* corresponds to the value of δR_s when the contact radii calculated using Eqs. (4.7) and (4.8) are equal. Solving this transcendental equation numerically yields $C_* \approx 3.2$.

Fig. 8b shows a comparison between analytically calculated indentation force–depth curves and the numerical solutions to the nonlinear problem. In this case, the curve is intrinsically nonlinear due to the varying contact radius. The good agreement when $\delta \lesssim 0.1$ demonstrates that the linearized theory might be used to interpret the spherical indentation experiment on cell membranes and 2D materials (Cellini et al., 2018; Mandriota et al., 2019). Additionally, Fig. 8b reveals a trend similar to that in Fig. 3b: as pre-tension increases, the region outside the contact area becomes increasingly significant (as suggested by the overlap of the red dashed and black dashed curves), allowing us to disregard the repulsive force stored in the contact region when pretension is sufficiently large.

5. Multilayer structures

Motivated by angstrom indentation on few-layer 2D materials in Gao et al. (2015, 2018), we replicate and stack the previously discussed elastic sheet-vdW foundation system in the vertical direction. A multilayer structure is thus formed (as shown in Fig. 9a), where each layer has the same bending stiffness B, pre-tension γ, and is connected to the layer below through linearized vdW interactions of stiffness K_{vdW}. Such

structures, aka. vdW materials, have attracted great interest in recent years, as the stacking of 2D materials provides a novel platform for advanced electronic devices (Dai et al., 2019, 2020). In this section, we propose to describe the punch indentation response of such a multilayer structure.

5.1. Numerical approach

For multilayer structures, we still use Föppl–von Kármán Eqs. (2.7) and (2.8) to describe the response of each layer (note that it makes no significant difference by using nonlinear foundation such as Eq. (3.4) when dealing with indentation stiffness). However, additional challenges arise in handling the boundary conditions: except for the top layer, the first displacement boundary condition in Eq. (3.5) is unknown. This missing boundary condition prevents us from solving the thin sheet deflection in one step, so we adopt the method of Newton–Raphson iteration instead. Specifically, the deflection at the center of the nth layer (counting from top to bottom) is denoted as δ_n, with the total forces from the upper and lower interactions as F_n^+ and F_n^-. clearly, $F_n^- = F_{n+1}^+$, and in the final equilibrium state, we expect $\Delta F_n = F_n^+ - F_n^- = 0$.

To avoid matching the boundary conditions near the indenter edge and simplify our numerical calculations, a spring with known stiffness is introduced between the cylindrical indenter and the uppermost sheet. When this spring is sufficiently stiff (at least $K_{\text{spring}} = 10^4$ in the code), it effectively becomes a Dirichlet boundary condition, corresponding to the prescribed indentation depth, but also make δ_1 unknown. We start with an initial estimation of $\delta_n^{(0)}$ and then calculate the correction vector according to the following equation:

$$\begin{pmatrix} \Delta\delta_1 \\ \Delta\delta_2 \\ \vdots \\ \Delta\delta_n \end{pmatrix} = -J^{-1} \begin{pmatrix} \Delta F_1 \\ \Delta F_2 \\ \vdots \\ \Delta F_n \end{pmatrix} \tag{5.1}$$

where Jacobian J is an $n \times n$ matrix whose elements are defined as $J_{ij} = \frac{\partial \Delta F_i}{\partial \delta_j}$ (here the partial derivatives are calculated by finite difference). Eq. (5.1) allows us to update the initial estimation: $\delta_n^{(i+1)} = \delta_n^{(i)} + \Delta\delta_n$, and the iteration procedure repeats until final convergence is achieved ($\Delta F_n \leq 1/1000 F_1$). We provide the matlab code for the calculation of multilayer indentation in GitHub.

5.2. Approximate methods

For an n-layered sheet-foundation system, the coupling of the deformation between layers makes it difficult to derive an completed

(a)

(b)
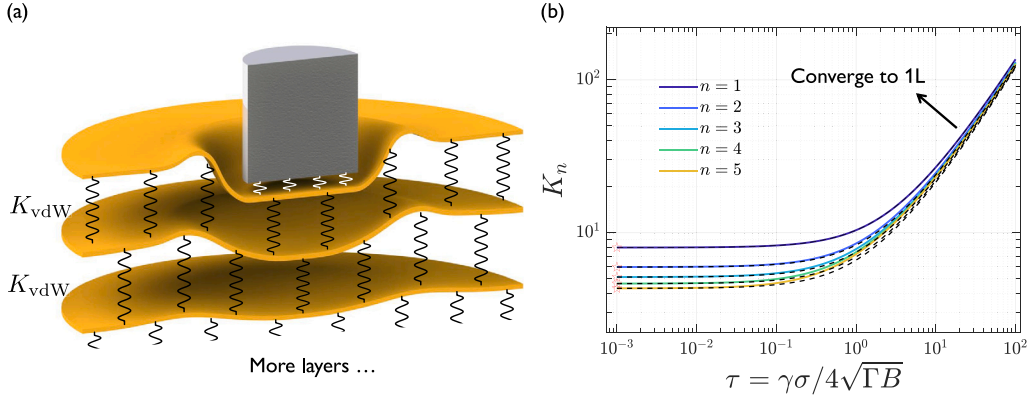
Fig. 9. (a) Schematic illustration of punch indentation on a multilayer structure. The white spring between the indenter and the sheet is fictitious for the convenience of numerical calculation. (b) The indentation stiffness as a function of pre-tension under point load. The black dashed curves represent the theoretical predictions given by "point model" discussed in the main text, whose error with numerical results (solid curves) is shown in Fig. 10. The star-shaped markers represent the numerical indentation stiffness K_n with low pre-tension, the fitting results of $(K_n/K_1)^2$ yields the selection of correction parameter α_n shown in Eq. (5.4), clearly $K_1 = 8$ according to Eq. (3.20).

analytical solution for indentation stiffness. However, given the thorough understanding of the single-layer sheet system in Section 3, we try to approximate the multilayer indentation problem as a single-layer case. In other words, the hope is to effectively reduce a n-layer indentation problem with interlayer spring stiffness K_{vdW} into a single-layer case with an effective vdW stiffness $K_{eff}(n)$, which relates to K_{vdW} via

$$K_{eff}(n) = \alpha_n K_{vdW}, \tag{5.2}$$

where α_n is a correction parameter to be determined. To remain consistent with the dimensionless form shown in Eq. (2.6), we also need to apply the following equivalent adjustments to the indenter radius and pre-tension using α_n:

$$\eta_{eff} = \alpha_n^{1/4} \eta \quad \text{and} \quad \tau_{eff} = \alpha_n^{-1/2} \tau \tag{5.3}$$

To clarify again, η, τ is nondimensionalized by K_{vdW}, and η_{eff}, τ_{eff} is nondimensionalized by $K_{eff}(n)$. With this approach, as long as α_n is chosen appropriately, by substituting all variables with their equivalent counterparts according to Eqs. (5.2) and (5.3), results for single-layer indentation from Section 3 can be applied to analyze the indentation stiffness and its asymptotic behavior of multilayer structures. Next, we discuss how α_n is selected.

The idea is to ensure that this equivalent approach with α_n captures the correct asymptotic behavior of the system under both small and large indenter sizes. In the case of small indenter radii where the indentation stiffness is controlled by K_{out}, equation (3.18) for the single-layer system has suggested the indentation stiffness $\propto K_{vdW}^{1/2}$ at the limit of $\tau \to 0$. Therefore, we determine α_n by the square of the ratio of the numerically calculated indentation stiffness of n-layer system to that of the single-layer case (extra explanations can be found in Fig. 9):

$$\alpha_n \approx (5.8063\, n^{-0.6223} + 2.1985)^2/64. \tag{5.4}$$

As such, the effective model can capture the asymptotic behavior of indentation stiffness in the limit of $\tau \to 0$, as shown in Fig. 9b. We refer to this model as the "point model" in the following text. Interestingly, this point model also works well in the regime of $\tau \gg 1$. The reason is that as the pre-tension increases, the indentation stiffness would be instead controlled by τ, making $K_{eff}(n)$ and hence α_n not important. Therefore, as suggested by Fig. 9b where the numerical solutions (solid curves) closely match the predictions of the point model (dashed curves), the point model simplifies the analysis without significantly sacrificing accuracy.

For large indenter radii, the region inside the indenter becomes more significant (the same trend as shown in Fig. 3b). In this region, all

layers are compressed "equally", allowing the problem to be directly simplified as a series of springs (referred to as "spring model" in the following text), i.e.,

$$\alpha_n = 1/n,$$

which leads to $\tau_{eff} = n^{1/2}\tau$ and $\eta_{eff} = n^{-1/4}\eta$.

It is foreseeable that this approximation will eventually become inaccurate when the pre-tension becomes exceedingly large; however, this typically falls beyond the range of pre-tension that we are concerned with. Fig. 10a shows the indentation stiffness as a function of pre-tension for $\eta = 100$, where we observe good agreement between the numerical solution (solid curves) and the theoretical prediction from spring model(dashed curves) when $\tau \leq 100$.

To further explore the applicability of the two models for intermediate indenter radii, Fig. 10b presents the maximum error of indentation stiffness between the theoretical and numerical solutions at different indenter radii. The error is calculated within the range of $\tau = 0.001$ to $\tau = 100$. Hence, by applying the point model when $\eta \ll 1$ and the spring model when $\eta \gg 1$, the maximum error in predicting indentation stiffness across five orders of magnitude of pre-tension remains below 10%. This confirms the validity of this simplified theoretical framework. In addition, we observe a "jump" in the slope of the curves in Fig. 10b, which is not due to numerical errors, as we have verified the independencies on computational grids and the stiffness of the fictitious spring. Instead, it arises because our study on multilayer indentation adopts an equivalent approach designed for different asymptotic regimes, without accounting for the complex deformation of the underlying films. Therefore, in regions where each model is not applicable, the error inevitably increases rapidly. Also, the position where the jump appears for the two models differs slightly (with the dashed line's jump at a later point). This may be due to differences in the mechanisms and locations of maximum error for the two models. The error of the point model is well-controlled under both small and large pre-tensions as discussed, while the maximum error of the spring model consistently occurs at maximum pre-tension. As shown in Fig. A.11b in the appendix, the two models exhibit similar positions in transition points for average errors.

6. Concluding remarks

6.1. Apparent stiffness

This paper has systematically analyzed the indentation force–depth relationship for a single-layer sheet on an elastic foundation. In particular, a set of analytical solutions have been derived for both punch
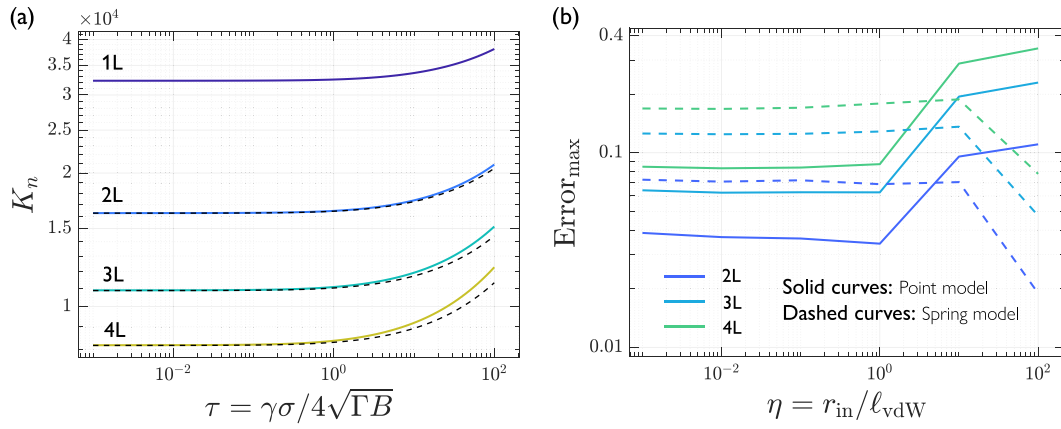
Fig. 10. (a) Comparison between the numerical indentation stiffness (solid curves) and predictions from the "spring model" for an indenter radius of $\eta = 100$. (b) Maximum error (calculated within the range of $\tau = 0.001$ to $\tau = 100$) between the numerical solution and the indentation stiffness predicted by the two models for different indenter radii. The mean error (which is smaller) is shown in Fig. A.11(b).

and spherical indenters, when the foundation could be linearized under small deflections. For a punch indenter, a linear force–displacement relationship is consistently observed when the indentation depth $\delta \ll \delta_c$, where δ_c, due to the geometrical nonlinearity in the thin sheet, depends on the pre-tension τ and the dimensionless parameter $\mathcal{K}$:

$$\delta_c = \begin{cases} \mathcal{K}^{-1/2} & \text{for } \tau \ll 1, \\ \tau \mathcal{K}^{-1/2} & \text{for } \tau \gg 1, \end{cases} \tag{6.1}$$

The asymptotic behavior of the corresponding indentation stiffness depends on the relative magnitude of the dimensionless indenter radius η and pre-tension τ, and is summarized as follows:

$$\text{When} \quad \tau \ll 1, \quad K_{\text{out}} \sim \begin{cases} 8 & \text{for } \eta \ll 1, \\ 2\sqrt{2}\pi\eta & \text{for } \eta \gg 1, \end{cases} \tag{6.2}$$

whilst

$$\text{when} \quad \tau \gg 1, \quad K_{\text{out}} \sim \begin{cases} 2\pi \dfrac{\tau}{\ln \tau} & \text{for } \eta \ll \tau^{-1/2}, \\ 2\pi \dfrac{\tau}{\ln\left(\sqrt{\tau}/\eta\right)} & \text{for } \tau^{-1/2} \ll \eta \ll \tau^{1/2}, \\ 2\pi\eta \left[\dfrac{1}{\sqrt{\tau}} + \sqrt{\tau} \right] & \text{for } \eta \gg \tau^{1/2}. \end{cases} \tag{6.3}$$

As the dimensionless indentation depth $\delta \to 1$, the short-range repulsive force of the van der Waals substrate causes a singularity in the force–displacement relationship of the following form:

$$\mathcal{F} \sim \begin{cases} (1-\delta)^{-4}, & \text{for } \eta \ll (1-\delta)^{5/2} \ll 1, \\ (1-\delta)^{-9}, & \text{for } (1-\delta)^{5/2} \ll \eta \ll 1. \end{cases} \tag{6.4}$$

For a spherical indenter, the movable contact boundary introduces additional nonlinearity, suggesting a nonlinear force–depth relationship even when $\delta \ll \delta_c$. However, when the pre-tension $\tau \ll 1$, the contact radius, implicitly determined by Eq. (4.4), can be largely simplified with δR_s serving as the key parameter:

$$\eta \sim \begin{cases} \sqrt{\delta R_s} - \sqrt{2} & \text{for } \delta R_s \gg 3.2, \\ e^{-\pi/\delta R_s} & \text{for } \delta R_s \ll 3.2. \end{cases} \tag{6.5}$$

For the multilayer indentation problem, we reduce a n-layer indentation problem with interlayer spring stiffness K_{vdW} into a single-layer case with an effective vdW stiffness $K_{\text{eff}}(n) = \alpha_n K_{\text{vdW}}$, Where α_n is a correction parameter obtained through fitting, and is related to the number of layers via the following expression:

$$\alpha_n = \begin{cases} \left(5.8063\, n^{-0.6223} + 2.1985\right)^2 / 64 & \text{for} \quad \eta \ll 1, \\ 1/n & \text{for} \quad \eta \gg 1. \end{cases} \tag{6.6}$$

by utilizing the equivalent pre-tension and indenter radius: $\tau_{\text{eff}} = \alpha_n^{-1/2}\tau$ and $\eta_{\text{eff}} = \alpha_n^{1/4}\eta$, we can analyze multilayer indentation based on the analytical results from single-layer indentation.

6.2. Conclusion

This paper has developed a theoretical model for the indentation of elastic sheets on mattress foundations. Starting from the linearized von Kármán equations and foundations, we systematically discussed the existence and analytical expression of indentation stiffness for punch and spherical indenters, showing excellent agreement with numerical results. Additionally, we presented asymptotic results for the indentation stiffness of punch indentation under different regimes of pre-tensions and indenter radii. These behaviors arose from the different dominance of three characteristic lengths ℓ_γ, ℓ_B, and $\ell_{B\gamma}$ in different regions of the sheet. Based on these results, we determined when pre-tension and indenter radius could be safely neglected at different scales: in the dimensionless framework used in this paper, pre-tension could be ignored when $\tau \ll 1$, and the indenter radius could be ignored when $\eta \ll \min\{\tau^{-1/2}, 1\}$, implying that the impact of indenter radius must be treated carefully at large pre-tensions. For multilayer systems, we introduced an equivalent foundation stiffness to extend the single-layer analysis approach, which proved surprisingly effective. In conclusion, this study provided a quantitative understanding of how pre-tension and indenter radius affect indentation stiffness, offering valuable insights for interpreting indentation experiments on small-scale materials and structures.

CRediT authorship contribution statement

Erteng Chen: Writing – original draft, Validation, Methodology, Investigation, Formal analysis. **Zhaohe Dai:** Writing – review & editing, Validation, Supervision, Methodology, Investigation, Formal analysis, Conceptualization.

Declaration of competing interest

The authors declare that they have no known competing financial interests or personal relationships that could have appeared to influence the work reported in this paper.
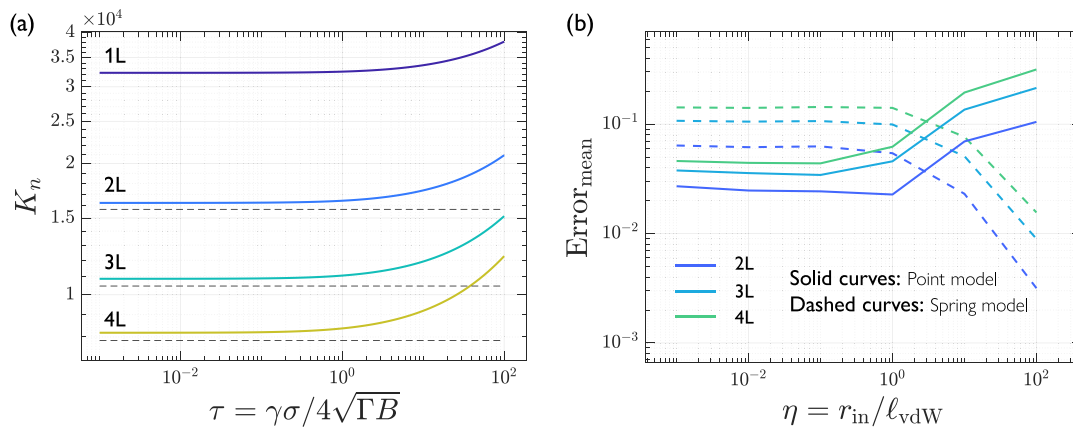
Acknowledgments

Fig. A.11. (a) Comparison between the numerical solution for indentation stiffness (solid curves) and $K_{\text{in}} = \pi \eta_{\text{eff}}^2$ (dashed curves) with the spring model for an indenter radius of $\eta = 100$. (b) Mean error (calculated within the range of $\tau = 0.001$ to $\tau = 100$) between the numerical solution and the indentation stiffness predicted by the two models for different indenter radii.

Appendix. Demonstration of the necessity of the multi-layer indentation model

In Section 5.2, we proposed that when the indenter radius is large, the influence of K_{in} is more significant, so $K_{\text{vdW}}^n = K_{\text{vdW}}/n$ is used as the equivalent foundation stiffness. This idea makes us raise a question: Is K_{in} itself sufficient to describe the indentation stiffness, and is it still meaningful to discuss the asymptotic behavior of K_{out}? Fig. A.11 shows the comparison between the numerical indentation stiffness curve and $K_{\text{in}} = \pi \eta_{\text{eff}}^2$ curve when $\eta = 100$. We note that even when $\tau \ll 1$, using only K_{in} to explain the indentation stiffness is not accurate enough, which further proves the necessity of our equivalent model that includes both K_{in} and K_{out}.

Data availability

Matlab code for indentation of multilayer structure is available in GitHub.

References

Ares, P., Wang, Y.B., Woods, C.R., Dougherty, J., Fumagalli, L., Guinea, F., Davidovitch, B., Novoselov, K.S., 2021. Van der waals interaction affects wrinkle formation in two-dimensional materials. Proc. Natl. Acad. Sci. 118 (14), e2025870118.

Argatov, I., Mishuris, G., Argatov, I., Mishuris, G., 2015. Deformation of a thin bonded transversely isotropic elastic layer. Contact Mech. Articul. Cartil. Layers: Asymptot. Model. 1–18.

Awang, M., Khalili, A.A., Pedapati, S.R., 2019. A review: Thin protective coating for wear protection in high-temperature application. Metals 10 (1), 42.

Barber, J.R., 2018. Contact Mechanics. vol. 20, Springer.

Bhattacharya, A., Nix, W., 1988. Analysis of elastic and plastic deformation associated with indentation testing of thin films on substrates. Int. J. Solids Struct. 24 (12), 1287–1298.

Blees, M.K., Barnard, A.W., Rose, P.A., Roberts, S.P., McGill, K.L., Huang, P.Y., Ruyack, A.R., Kevek, J.W., Kobrin, B., Muller, D.A., et al., 2015. Graphene kirigami. Nature 524 (7564), 204–207.

Box, F., Jacquemot, C., Adda-Bedia, M., Vella, D., 2020. Cloaking by coating: how effectively does a thin, stiff coating hide a soft substrate? Soft Matter 16 (19), 4574–4583.

Box, F., Vella, D., Style, R.W., Neufeld, J.A., 2017. Indentation of a floating elastic sheet: geometry versus applied tension. Proc. R. Soc. A 473 (2206), 20170335.

Cao, G., Gao, H., 2019. Mechanical properties characterization of two-dimensional materials via nanoindentation experiments. Prog. Mater. Sci. 103, 558–595.

Cellini, F., Lavini, F., Cao, T., de Heer, W., Berger, C., Bongiorno, A., Riedo, E., 2018. Epitaxial two-layer graphene under pressure: Diamene stiffer than diamond. FlatChem 10, 8–13.

Chandler, T.G., Vella, D., 2020a. Indentation of suspended two-dimensional solids: The signatures of geometrical and material nonlinearity. J. Mech. Phys. Solids 144, 104109.

Chandler, T.G., Vella, D., 2020b. Validity of Winkler's mattress model for thin elastomeric layers: beyond Poisson's ratio. Proc. R. Soc. A 476 (2242), 20200551.

Chen, E., Dai, Z., 2023. Axisymmetric peeling of thin elastic films: A perturbation solution. J. Appl. Mech. 90 (10).

Dai, Z., 2024. Analytical solutions for circular elastic membranes under pressure. J. Appl. Mech. 91 (8), 081002.

Dai, Z., Liu, L., Zhang, Z., 2019. Strain engineering of 2D materials: issues and opportunities at the interface. Adv. Mater. 31 (45), 1805417.

Dai, Z., Lu, N., 2021. Poking and bulging of suspended thin sheets: Slippage, instabilities, and metrology. J. Mech. Phys. Solids 149, 104320.

Dai, Z., Lu, N., Liechti, K.M., Huang, R., 2020. Mechanics at the interfaces of 2D materials: Challenges and opportunities. Curr. Opin. Solid State Mater. Sci. 24 (4), 100837.

Dai, Z., Rao, Y., Lu, N., 2022. Two-dimensional crystals on adhesive substrates subjected to uniform transverse pressure. Int. J. Solids Struct. 257, 111829.

Davidovitch, B., Guinea, F., 2021. Indentation of solid membranes on rigid substrates with van der Waals attraction. Phys. Rev. E 103 (4), 043002.

Derjaguin, B.V., Muller, V.M., Toporov, Y.P., 1975. Effect of contact deformations on the adhesion of particles. J. Colloid Interface Sci. 53 (2), 314–326.

Di Leo, C.V., Luk-Cyr, J., Liu, H., Loeffel, K., Al-Athel, K., Anand, L., 2014. A new methodology for characterizing traction-separation relations for interfacial delamination of thermal barrier coatings. Acta Mater. 71, 306–318.

Dillard, D.A., Mukherjee, B., Karnal, P., Batra, R.C., Frechette, J., 2018. A review of Winkler's foundation and its profound influence on adhesion and soft matter applications. Soft Matter 14 (19), 3669–3683.

Ding, Y., Liang, X.M., Li, C.Y., Wang, G.F., 2023. Surface effects on the spherical indentation of biological film/substrate structures. J. Phys. D: Appl. Phys. 56 (38), 385307.

Feng, H., Zhao, C., Tan, P., Liu, R., Chen, X., Li, Z., 2018. Nanogenerator for biomedical applications. Adv. Heal. Mater. 7 (10), 1701298.

Freund, L.B., Suresh, S., 2004. Thin Film Materials: Stress, Defect Formation and Surface Evolution. Cambridge University Press.

Gao, Y., Cao, T., Cellini, F., Berger, C., De Heer, W.A., Tosatti, E., Riedo, E., Bongiorno, A., 2018. Ultrahard carbon film from epitaxial two-layer graphene. Nat. Nanotechnol. 13 (2), 133–138.

Gao, Y., Kim, S., Zhou, S., Chiu, H.C., Nélias, D., Berger, C., De Heer, W., Polloni, L., Sordan, R., Bongiorno, A., et al., 2015. Elastic coupling between layers in two-dimensional materials. Nat. Mater. 14 (7), 714–720.

Gao, W., Xiao, P., Henkelman, G., Liechti, K.M., Huang, R., 2014. Interfacial adhesion between graphene and silicon dioxide by density functional theory with van der Waals corrections. J. Phys. D: Appl. Phys. 47 (25), 255301.

Hao, S., Huang, R., Rodin, G.J., 2024. Constitutive models for confined elastomeric layers: Effects of nonlinearity and compressibility. Mech. Mater. 190, 104912.

Hwang, G.T., Byun, M., Jeong, C.K., Lee, K.J., 2015. Flexible piezoelectric thin-film energy harvesters and nanosensors for biomedical applications. Adv. Heal. Mater. 4 (5), 646–658.

Israelachvili, J.N., 2011. Intermolecular and Surface Forces. Academic Press.

Kerr, A.D., 1964. Elastic and viscoelastic foundation models. J. Appl. Mech. 31 (3), 491–498.

Li, H., Dai, Z., 2025. Adhesion of elastic microbeams on thin deformable substrates. Eng. Fract. Mech. 313, 110634.

Li, H., Yu, C., Dai, Z., 2024a. Regimes in the axisymmetric stiction of thin elastic plates. Int. J. Mech. Sci. 284, 109740.

Li, J., Zhang, G., Wang, L., Dai, Z., 2024b. Indentation of a plate on a thin transversely isotropic elastic layer. Acta Mech. Solida Sin. 1–10.

Liu, Y., Wei, Y., Chen, P., 2019. Characterization of mechanical properties of two-dimensional materials mounted on soft substrate. Int. J. Mech. Sci. 151, 214–221.

Mandriota, N., Friedsam, C., Jones-Molina, J.A., Tatem, K.V., Ingber, D.E., Sahin, O., 2019. Cellular nanoscale stiffness patterns governed by intracellular forces. Nat. Mater. 18 (10), 1071–1077.

Mansfield, E.H., 1989. The bending and stretching of plates.

Nase, M., Langer, B., Baumann, H.J., Grellmann, W., Geißler, G., Kaliske, M., 2009. Evaluation and simulation of the peel behavior of polyethylene/polybutene-1 peel systems. J. Appl. Polym. Sci. 111 (1), 363–370.

Raut, H.K., Ganesh, V.A., Nair, A.S., Ramakrishna, S., 2011. Anti-reflective coatings: A critical, in-depth review. Energy Env. Sci. 4 (10), 3779–3804.

Wang, X., Chen, E., Wu, Q., Yuan, X., Zhang, T., Zhu, S., Dai, Z., Gao, Y., 2025b. Probing the elastic coupling at van der waals interfaces of two-dimensional materials. Phys. Rev. B 111, 125418.

Wang, G., Dai, Z., Xiao, J., Feng, S., Weng, C., Liu, L., Xu, Z., Huang, R., Zhang, Z., 2019. Bending of multilayer van der Waals materials. Phys. Rev. Lett. 123 (11), 116101.

Wang, P., Liechti, K.M., Huang, R., 2016. Snap transitions of pressurized graphene blisters. J. Appl. Mech. 83 (7), 071002.

Wang, W., Wei, Z., Li, Y.J., You, J., Li, X., He, J., Mao, H., Jin, J., Sun, L., Dai, Z., 2025a. Multifunctional complementary field-effect transistors based on MoS2/SWNTs heterostructures. Appl. Phys. Lett. 126 (2).

Winkler, E., 1867. Die Lehre von der Elasticitaet und Festigkeit: mit besonderer Rücksicht auf ihre Anwendung in der Technik, für polytechnische Schulen, Bauakademien, Ingenieure, Maschinenbauer, Architecten, etc. H. Dominicus.

Yang, N.J., Hinner, M.J., 2015. Getting across the cell membrane: an overview for small molecules, peptides, and proteins. Site- Specif. Protein Labeling: Methods Protoc. 29–53.

Yu, C., Dai, Z., 2024. Premature jump-to-contact with elastic surfaces. J. Mech. Phys. Solids 193, 105919.

Yu, C., Zeng, W., Wang, B., Cui, X., Gao, Z., Yin, J., Liu, L., Wei, X., Wei, Y., Dai, Z., 2025. Stiffer is stickier: Adhesion in elastic nanofilms. Nano Lett. 25 (5), 1876–1882.

Yuan, W., Ding, Y., Wang, G., 2023. Universal contact stiffness of elastic solids covered with tensed membranes and its application in indentation tests of biological materials. Acta Biomater. 171, 202–208.

Zhang, H., Huang, J., Wang, Y., Liu, R., Huai, X., Jiang, J., Anfuso, C., 2018. Atomic force microscopy for two-dimensional materials: A tutorial review. Opt. Commun. 406, 3–17.

Zhang, Q., Witten, T.A., 2007. Microscopic wrinkles on supported surfactant monolayers. Phys. Rev. E 76 (4), 041608.

Zschieschang, U., Waizmann, U., Weis, J., Borchert, J.W., Klauk, H., 2022. Nanoscale flexible organic thin-film transistors. Sci. Adv. 8 (13), eabm9845.